ADVANCED MATERIALS

www.advmat.de

Dual Functions of Crystallization Control and Defect Passivation Enabled by Sulfonic Zwitterions for Stable and Efficient Perovskite Solar Cells

*Xiaopeng Zheng, Yehao Deng, Bo Chen, Haotong Wei, Xun Xiao, Yanjun Fang, Yuze Lin, Zhenhua Yu, Ye Liu, Qi Wang, and Jinsong Huang**

Uniform and high-electronic-quality perovskite thin films are essential for high-performance perovskite devices. Here, it is shown that the 3-(decyldimethylammonio)-propane-sulfonate inner salt (DPSI), which is a sulfonic zwitterion, plays dual roles in tuning the crystallization behavior and passivating the defects of perovskites. The synergistic effect of crystallization control and defect passivation remarkably suppresses pinhole formation, reduces the charge trap density, and lengthens the carrier recombination lifetime, and thereafter boosts the small-area (0.08 cm^2) planar perovskite device efficiency to 21.1% and enables a high efficiency of 18.3% for blade-coating large-area (1 cm^2) devices. The device also shows good light stability, which remains at 88% of the initial efficiency under continuous unfiltered AM 1.5G light illumination for 480 h. These findings provide an avenue for simultaneous crystallization control and defect passivation to further improve the performance of perovskite devices.

Organic–inorganic halide perovskites (OIHPs) exhibit impressive optoelectronic properties, including large absorption coefficient, long carrier recombination lifetime, long carrier diffusion length, and are emerging as promising candidates for the low-cost and high-performance photovoltaics (PVs) and other optoelectronic applications.[1–9] Benefiting from these favorable attributes, the power conversion efficiency (PCE) of perovskite PV has been rapidly improved from 3.8% to a certified value of 23.3%[10] over the past several years.[11,12] Meanwhile, an entire range of techniques used to produce efficient perovskite solar cells has been developed. The techniques that enable rapid PCE advances are based not only on the optimization of the film morphology by tuning the perovskite crystallization behaviors,[13–16] but also benefiting from passivating nonradiative charge recombination centers with functional molecules, metal ions, and halide ions.[17–28] Bi et al. reported that poly(methyl methacrylate) (PMMA) could template perovskite nucleation and crystal growth.[14] Yang et al. showed that the introduction of additional iodide ions into the organic cation solution decreased the concentration of deep-level defects, which in return resulted in a certified record PCE of 22.1% for OIHP devices.[12] To slow down the perovskite crystallization, and improve grain size and crystallinity, the solvent additives such as dimethyl sulfoxide (DMSO), *N*-methyl-2-pyrrolidone (NMP), and 1,8-diiodooctane (DIO) were added into the precursor solution to form the complexes with PbI_2, and these complexes can be slowly converted into perovskite by an intramolecular exchanging process.[29–32] However, these solvent additives could be evaporated during the high-temperature annealing process and thus play no defect passivation functions after the OIHP films dry. It has been shown that the surfaces and grain boundaries of solution-processed OIHP films can be a reservoir of trap states or deep defect states which dominate the nonradiative charge recombination and pull down the open-circuit voltage (V_{OC}) of perovskite devices, and also initiate the perovskite film degradation.[33–40] Therefore, reducing the number of defects at film surfaces and grain boundaries is necessary to enhance both efficiency and stability of perovskite solar cells.[34,38] It is still challenging to realize the synergistic effect of the morphology controlling and trap states passivation for further enhancement of the PCE and stability of OIHP devices.

In this study, we introduce the sulfonic zwitterion to simultaneously control the perovskite crystallization and passivate defect states of OIHP thin films, which enhances the small-area (0.08 cm^2) and large-area (1 cm^2) planar perovskite device efficiency to 21.1% and 18.3%, respectively. The results highlight the synergetic effect of controlling crystallization and trap passivation for improving perovskite devices.

It is clear that the ligands containing sulfonic group, such as DMSO, can form complex with lead ions in the perovskite precursor, which significantly slows down the perovskite

X. Zheng, Dr. Y. Fang, Prof. J. Huang
Department of Mechanical and Materials Engineering
University of Nebraska-Lincoln
Lincoln, NE 68588, USA
E-mail: jhuang@unc.edu

Y. Deng, Dr. B. Chen, Dr. H. Wei, X. Xiao, Dr. Y. Lin, Dr. Z. Yu, Y. Liu, Q. Wang, Prof. J. Huang
Department of Applied Physical Sciences
University of North Carolina
Chapel Hill, NC 27599, USA

The ORCID identification number(s) for the author(s) of this article can be found under https://doi.org/10.1002/adma.201803428.

DOI: 10.1002/adma.201803428

crystallization and benefits for the high-quality film fabrication.[32] The 3-(decyldimethylammonio)-propane-sulfonate inner salt (DPSI) is a sulfonic zwitterion which contains a positively charged quaternary ammonium group, a negatively charged sulfonic group, and a long alkyl chain. It has been reported that amphiphilic surfactants could increase the adhesion of the perovskite ink to the substrate, and enable blading of high-efficiency perovskite modules.[41,42] Moreover, our previous study showed that the zwitterionic molecules could efficiently passivate the defects of perovskites, but this surface treatment strategy is lack of the function of the morphology tailoring.[28] Thus, the DPSI molecule, a sulfonic zwitterion, is potentially capable of assembling the function of crystallization tuning because of the surfactant nature and the lead coordination by the sulfonic group, together with the function of the defect passivation due to its zwitterionic structure.

To study the influence on the perovskite crystallization, we introduced a small amount of DPSI molecules (0.05 wt%) into the methylammonium (MA) lead iodide $MAPbI_3$ precursor solution and fabricated the perovskite thin film by a one-step spin-coating method. The formation of coordination bond between DPSI and lead ions of the perovskite can be proved by the Fourier transform infrared (FTIR) spectroscopy study. As shown in Figure S1 (Supporting Information), the peak appeared at 1029 cm^{-1} is attribute to the S=O stretch from the sulfonic group of DPSI. This peak shifted to 1010 cm^{-1}, which attributed to the coordination with the perovskite where the S=O may donate their lone unpaired electron to the empty orbitals of Pb^{2+}, which is in consistent with the strong interaction between the sulfonic group of the DMSO molecule and the lead ion in the perovskite precursor. It is widely proposed that applying an antisolvent during spin coating of precursor films causes rapid supersaturation of solution and thus quick nucleation.[12,14,17] During the $MAPbI_3$ film processing, the drying of the precursor solution first yields a yellow intermedium phase containing residual solvent (such as dimethyformamide (DMF) or DMSO). The subsequent uncontrolled fast-drying and rapid-crystallization process under the thermal annealing could cause morphological defects, such as pinholes, and a broad grain size distribution.[9,17,31]

As illustrated in **Figure 1**a, we propose that the DPSI molecules could attach on the surfaces of perovskite nucleus because

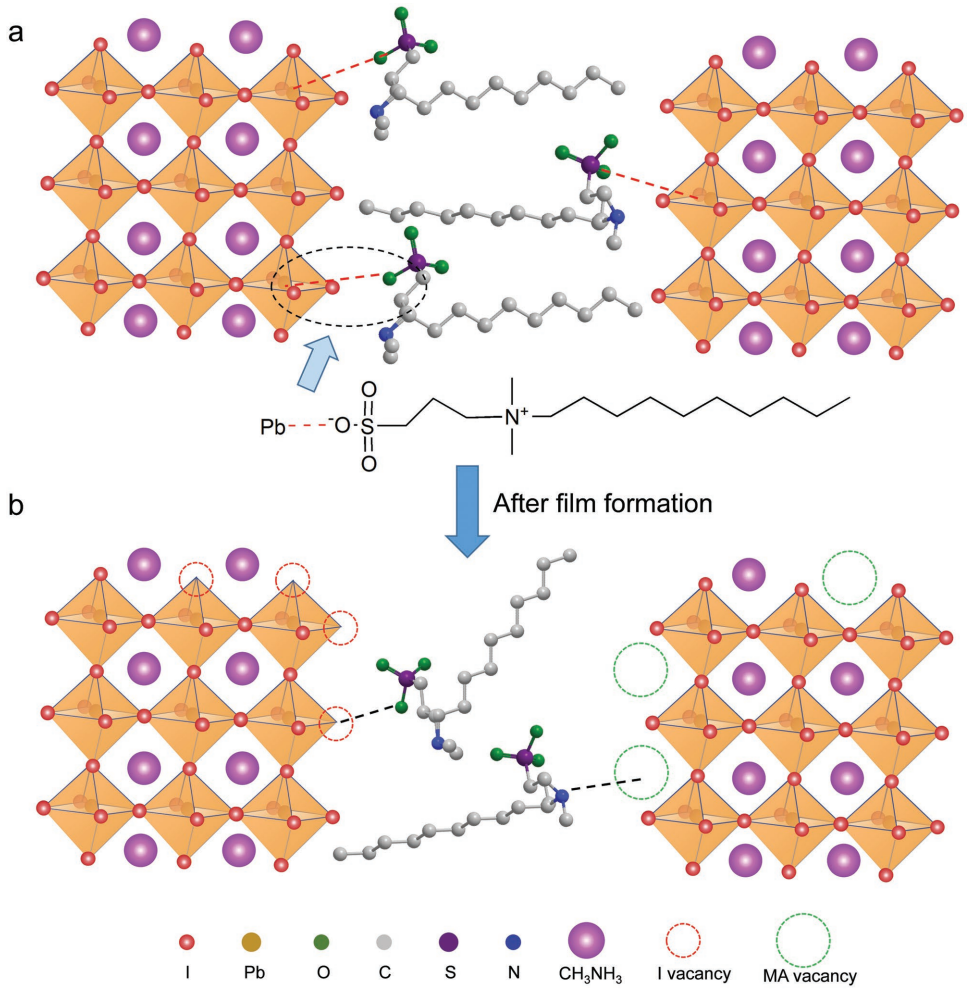

Figure 1. Schematic illustration of DPSI mediated perovskite growth and defect passivation. a) The DPSI molecules first attached on the surface of perovskite nucleus and precise control each grain growth to uniform size. b) The DPSI molecules were repelled to the grain boundaries and film surfaces after the perovskite film formation and passivate the defect states at grain boundaries and film surfaces.

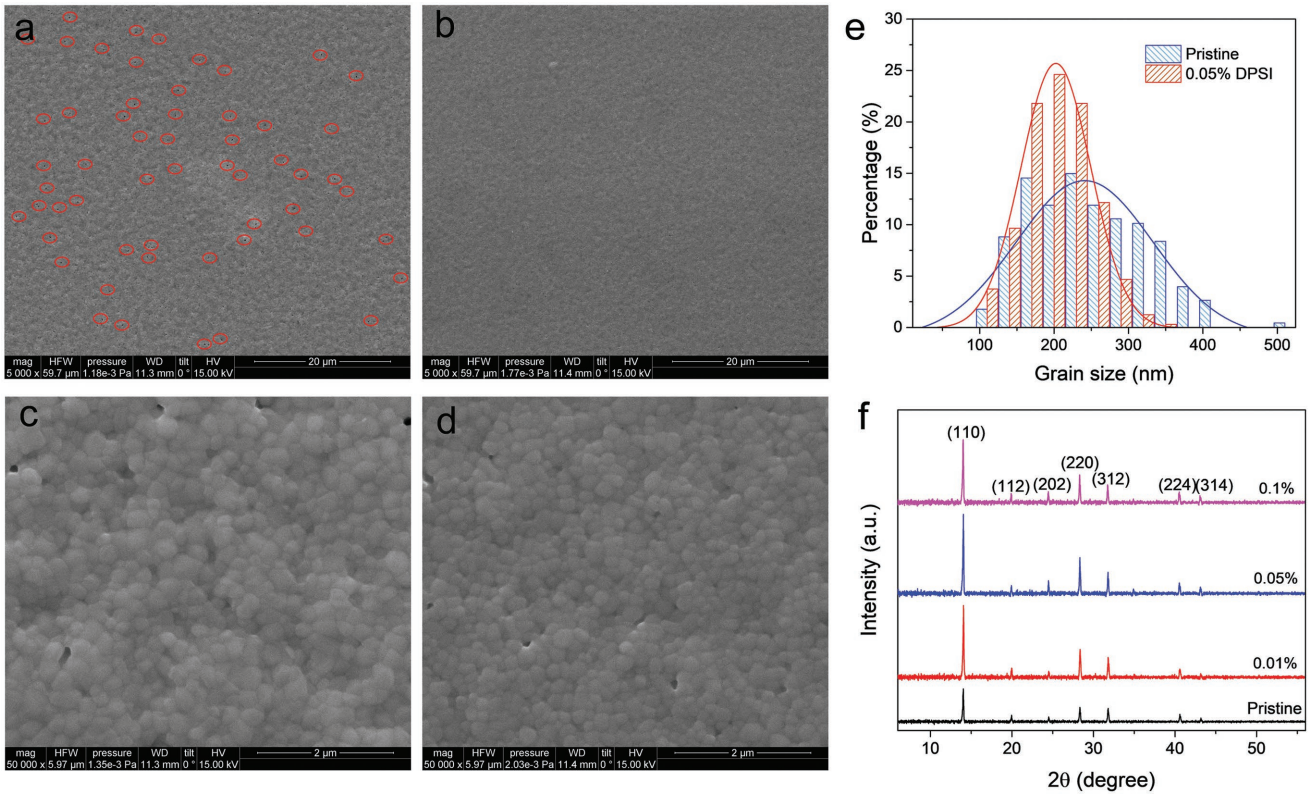

Figure 2. DPSI mediated perovskite thin film growth. a,b) Scanning electron microscopy (SEM) images of the $MAPbI_3$ films without and with adding 0.05% of the DPSI molecules, respectively. The pinholes are marked with the red circles. c,d) The enlarged SEM images of the $MAPbI_3$ films without and with adding 0.05% of the DPSI molecules, respectively. e) Grain size distributions calculated from ≈300 grains from the SEM images. The blue and red solid lines represent the Gaussian distribution fitting for the statistics of grain size. f) XRD patterns of pristine $MAPbI_3$ film and the film with DPSI.

of the strong coordination bonds between the DPSI and lead ions, and thereafter constrain the perovskite crystal growth and suppress the morphological defect formation during the processing of the perovskite film. After the perovskite film formation, the DPSI molecules can neutralize the charged defects at the surfaces and grain boundaries of the perovskite film using their positively and negatively charged components, as illustrated in Figure 1b.[28] **Figure 2**a,b shows the scanning electron microscopy (SEM) images of the $MAPbI_3$ films without and with adding of 0.05% DPSI molecules, respectively. The formation of pinholes was greatly suppressed for the films with DPSI in the precursor solution. The enlarged SEM images in Figure 2c,d show that the films with DPSI possess much more uniform grain size. The corresponding grain size distribution is summarized in Figure 2e. The average grain size of $MAPbI_3$ film with 0.05% DPSI is ≈203 nm, which is about 48 nm smaller than that of the pristine $MAPbI_3$ film, but the grain size distribution is much narrower. It indicates that the DPSI molecules retarded and well controlled each perovskite grain growth to uniform size and eventually construct a compact perovskite film. The grain size was further reduced, and some aggregation appeared when the DPSI concentration increased to 0.01%, as shown in Figure S2 (Supporting Information).

To explore the impact of the DPSI on the perovskite film crystal structure, we collected X-ray diffraction (XRD) patterns of the films with different DPSI concentrations and calculated the peak intensity ratio between (110) and (312), as shown in Figure 2f and in Figure S3 (Supporting Information), respectively. The result shows that, with increasing of the DPSI concentration to 0.05%, the (110) peak intensity and the ratio between the (110) and (312) peaks at 14.1 and 31.8 were increased, which may arise from the grain orientation change.

The p–i–n planar cell configuration used in this study was structured as poly[bis(4-phenyl)(2,4,6-trimethylphenyl)amine] (PTAA)/OIHPs/phenyl-C_{61}-butyric acid methyl ester (PCBM)/C_{60}/bathocuproine (BCP)/copper (Cu). Considering that the charge carrier extraction efficiency strongly depends on the amount of the insulating molecules that introduced into perovskite film, we first studied the effect of DPSI molecule concentration on the device performance. **Figure 3**a shows the photocurrent curves of perovskite devices with different amount of DPSI which were tuned by varying the concentration of DPSI in the $MAPbI_3$ precursor solution. The control device without DPSI showed typical performance with a short-circuit current density (J_{SC}) of 22.6 mA cm^{-2}, a V_{OC} of 1.08 V, a fill factor (FF) of 75.0%, and a PCE of 18.4%. When the DPSI concentration was increased to 0.01% and 0.05%, the V_{OC} was significantly increased to 1.10 and 1.12 V, respectively. The best $MAPbI_3$ devices were made by the precursor solution with 0.05% DPSI, exhibiting a significantly improved performance with a J_{SC} of 22.8 mA cm^{-2}, a V_{OC} of 1.12 V, an FF of 79.0%, and a PCE of 20.2%. We also checked the photocurrent hysteresis of the devices with 0.05% DPSI, and negligible photocurrent hysteresis was observed, as shown in Figure S4

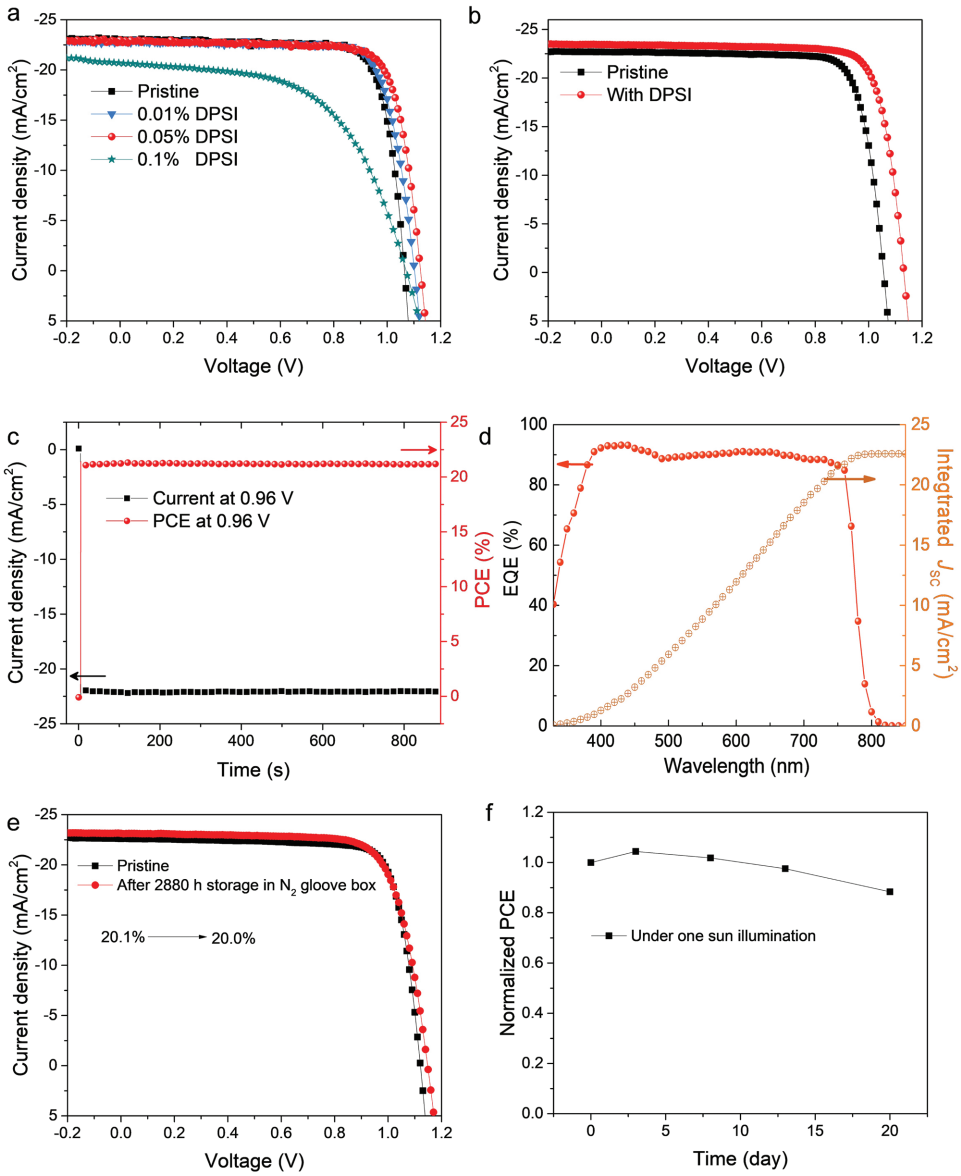

Figure 3. The photovoltaic characteristics of spin-coating planar perovskite devices. a) *J–V* characteristics of $MAPbI_3$ devices with different amounts of DPSI. b) *J–V* characteristics of $FA_{0.85}MA_{0.15}Pb(Br_{0.15}I_{0.85})_3$ devices with and without DPSI. c) Steady-state photocurrent and efficiency at the maximum power point (0.96 V) of the optimized $FA_{0.85}MA_{0.15}Pb(Br_{0.15}I_{0.85})_3$ device with DPSI. d) EQE and integrated J_{SC} for the optimized $FA_{0.85}MA_{0.15}Pb(Br_{0.15}I_{0.85})_3$ device with DPSI. e) *J–V* characteristics of $FA_{0.85}MA_{0.15}Pb(Br_{0.15}I_{0.85})_3$ device with DPSI before and after 2880 h storage in the nitrogen glove box under dark. f) Photovoltaic performance of encapsulated $FA_{0.85}MA_{0.15}Pb(Br_{0.15}I_{0.85})_3$ device with DPSI in an ambient environment under continuous AM 1.5G illumination as a function of storage time.

(Supporting Information). The performance enhancement was tentatively attributed to the improved film morphology and the passivated grain boundaries achieved by the dual functions of the DPSI molecules. The *J–V* curve in Figure 3a and the statistical result in Figure S5 (Supporting Information) show that further increasing DPSI concentration to 0.1% severely reduced the J_{SC}, V_{OC}, and FF, and the *J–V* curve, which indicates that the device with excess DPSI possesses high series resistance (R_S, 1494.9 Ω cm^2) that decreases the J_{SC} and FF. The R_S for the device without DPSI is 78.4 Ω cm^2. The underlying reason for the bad performance of the device with excess DPSI may because the increased thickness of the insulating layer surrounding the perovskite grains reduced electron tunneling rate.[43] To study whether DPSI impacts on the PV performance of the devices with different perovskite compositions, we fabricated formamidinium (FA)/MA mixed devices with composition of $FA_{0.85}MA_{0.15}Pb(I_{0.85}Br_{0.15})_3$. As shown in Figure 3b, the best performing $FA_{0.85}MA_{0.15}Pb(I_{0.85}Br_{0.15})_3$ device without DPSI yields a PCE of 19.1%, with a J_{SC} of 22.7 mA cm^{-2}, a V_{OC} of 1.06 V, and an FF of 80%. The champion $FA_{0.85}MA_{0.15}Pb(I_{0.85}Br_{0.15})_3$ device with 0.05% DPSI reached a PCE of 21.1%, with a J_{SC} of 23.3 mA cm^{-2}, a V_{OC} of 1.13 V, and an FF of 80%. An obvious V_{OC} enhancement from 1.06 to 1.13 V was observed for the devices with this perovskite

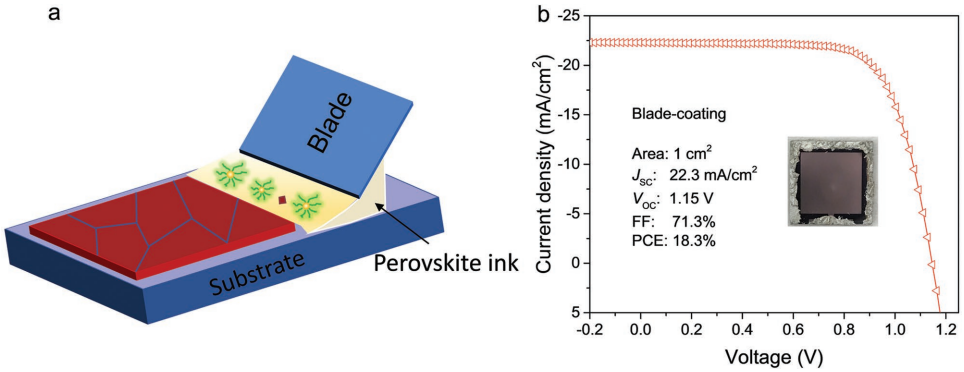

Figure 4. Blade-coating large-area device with DPSI. a) Schematic illustration of the blade coating of perovskite films with DPSI in the precursor ink. b) The photovoltaic characteristics of large-area $FA_{0.85}MA_{0.15}Pb(I_{0.85}Br_{0.15})_3$ device with DPSI.

composition. The stabilized PCE was measured to determine the real power output of the device by monitoring the photocurrent of the device under an applied bias at the maximum power point under AM 1.5G illumination. It exhibited a stabilized efficiency of 21.1% at the maximum power point (0.96 V) for testing over 2000 s, which matched well with the PCE value extracted from the *J*–*V* curve (Figure 3c). The external quantum efficiency (EQE) spectrum (Figure 3d) exhibited a broad region range from 400 to 760 nm with EQE well above 85% because of strong light absorption within the perovskite film, and the EQE reached 90% in some wavelength range of 400–450 nm, which is in accordance with the highest transparence peak of the indium–tin oxide (ITO) glass substrate. The EQE spectrum showed an integrated J_{SC} of 22.6 mA cm^{-2}, which agreed well with the *J*–*V* results. As shown in Figure S6 (Supporting Information), the statistics PCE values of 40 devices demonstrate the reproducibility and reliability of the performance enhancement by introducing of DPSI.

We examined the stability of unencapsulated devices stored in the dark in a glove box filled with nitrogen as well as encapsulated devices under AM 1.5G illumination in ambient condition. It was found that the devices maintained almost their original efficiency when stored in the nitrogen-filled glove box in the dark for 2880 h (4 months) (Figure 3e). The initial PV parameters for the device with DPSI are a J_{SC} of 22.6 mA cm^{-2}, a V_{OC} of 1.12 V, an FF of 79.4%, and a PCE of 20.1%. The PV parameters of the device after 2880 h storage are a J_{SC} of 23.1 mA cm^{-2}, a V_{OC} of 1.15 V, an FF of 75.3%, and a PCE of 20.0%. The real application requires perovskite solar cells to be stable under sun illumination. To evaluate the operational stability of devices with DPSI, we monitored the *J*–*V* characteristics of the encapsulated device under simulated AM 1.5G illumination without using an ultraviolet filter. The device with DPSI retained 88% of their initial performance after 480 h under continuous AM 1.5G illumination, as shown in Figure 3f. To convey the moisture stability information, we monitored the PCE of the unencapsulated device under the full spectrum of 1 sun light illumination with environmental humidity from 30% to 70% for 60 h, as shown in Figure S7 (Supporting Information). The result shows that the unencapsulated device retained 96% of their initial performance after 60 h test, indicating that the decent moisture stability of the device with DPSI. However, we believe that the encapsulation technology is paramount for the long-lived perovskite devices.

The pinhole-free perovskite films are essential for large-area devices. Here, we also evaluate the application of DPSI in large-area devices fabricated by blade coating, which is illustrated in **Figure 4**a. Blade coating is a scalable, simple, low-cost, solution-based thin film deposition technique that is compatible with the roll-to-roll fabrication process for the large-scale production of perovskite solar cell panels.[44–46] However, this method generally produced devices with lower PCE at lower yield than spin coating, because of the poorer film quality with pinholes.[31] We fabricated the large-area devices (1 cm^2) with the perovskite composition of $FA_{0.85}MA_{0.15}Pb(Br_{0.15}I_{0.85})_3$ by a blade-coating method with 0.04 wt% of DPSI added. As shown in Figure 4b, the PCE of the blade-coated large-area device with DPSI has reached 18.3%, with a J_{SC} of 22.3 mA cm^{-2}, a V_{OC} of 1.15 V, and an FF of 71.3%, which among the highest performance for large-area devices made by scalable methods. These results highlight the importance of sulfonic zwitterion as an addictive for preparation of high-quality perovskite films with good uniformity for scalable manufacturing of perovskite solar cell panels.

To obtain further insights into the origin of the performance enhancement for the device with DPSI, we performed thermal admittance spectroscopy (TAS) measurement to examine the trap density of states (tDOS) in the $MAPbI_3$ devices with and without DPSI.[47] As shown in **Figure 5**a, there was a relatively large density of defect states in the order of 1×10^{16} to 1×10^{20} m^{-3} in the devices without DPSI. The device with DPSI had six times smaller tDOS over trap depth from 0.35 to 0.4 eV. Our previous study of the tDOS in $MAPbI_3$ assigned deeper traps in the region of 0.40–0.52 eV to the defects at the film surface, and shallower trap states (0.35–0.40 eV) to the defects at grain boundaries.[7,24] The fact that tDOSs in both regions reduced indicates that DPSI molecules could efficiently passivate the trap states enriched both at the grain boundaries and at the film surfaces.

To study the charge carrier recombination dynamics, the time-resolved photoluminescence (TRPL) decay measurement was performed. The TRPL decay of the $MAPbI_3$ films on glass substrate showed biexponential decays composed of a fast and a long part (Figure 5c). The PL decay curves were fitted to a biexponential rate law

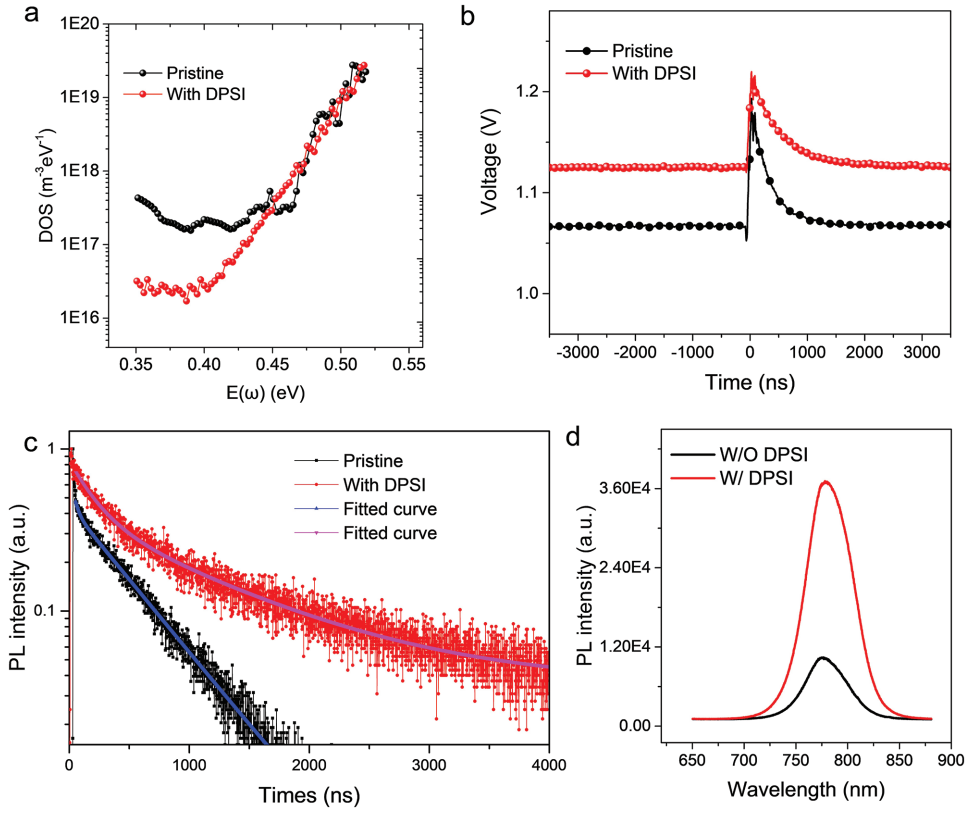

Figure 5. Defect passivation by DPSI. a) Trap density of states (tDOS) obtained by thermal admittance spectroscopy for $MAPbI_3$ devices without and with DPSI. b) Charge carrier lifetime of device with DPSI and control device without DPSI, determined from transient photovoltage (TPV) measurement under open-circuit condition. The *y*-axis shows the V_{OC} of the devices. c) Time-resolved photoluminescence (TRPL) decay of perovskite films with DPSI compared with control film without DPSI. The fitted curves are obtained by fitting the data using a biexponential rate law. The fluence and the excitation density were 2.0 nJ cm^{-2} and 4.07×10^{14} cm^{-3}, respectively. d) The steady-state PL spectra collected from the unpassivated region and passivation region on the $MAPbI_3$ film.

$$y = A_1 \exp\left(-t/\tau_1\right) + A_2 \exp\left(-t/\tau_2\right) + y_0 \quad (1)$$

where A_1 and A_2 are the relative amplitudes, and τ_1 and τ_2 are the lifetimes for the fast and slow decays, respectively. Previous studies assigned the decays to the recombination induced by defects.[9,14,32] The film with the DPSI exhibits fast and slow phase lifetimes of τ_1 = 317 ns (A_1 = 0.48) and τ_2 = 1632 ns (A_2 = 0.25), respectively. By contrast, the pristine sample without DPSI shows τ_1 = 42 ns (A_1 = 0.74) and τ_2 = 476 ns (A_2 = 0.45), respectively. This prolonged lifetime after DPSI passivation is attributed to strongly suppressed carrier trapping at surfaces and grain boundaries of the perovskite films, which is in consistent with the tDOS result.

To directly verify the passivation effect of DPSI, we measured the PL intensity of a same perovskite films on the passivated region and pristine region. The passivated region was created by drop coating of the DPSI toluene solution on the $MAPbI_3$ film. Figure 5d shows that the passivated region with DPSI-coated $MAPbI_3$ film presents a large rise in PL intensity in comparison to the region without DPSI passivation. TRPL and PL have been frequently applied to evaluate the quality of the perovskite films, but the measured lifetime does not correspond to the charge recombination lifetime in the device under open-circuit conditions. To find out how passivation affects the charge recombination process in the devices under operating conditions, transient photovoltage (TPV) measurement was conducted using the $MAPbI_3$ perovskite device. The devices were soaked under AM 1.5G simulated illumination, and attenuated laser pulses (337 nm, 4 ns) were applied to cause a small disturbance to open-circuited devices, which triggered a small transient photovoltaic signal. As seen in Figure 5b, the TPV transient lifetime of the device with DPSI passivation was increased from 330 ns for the device without DPSI to 536 ns for the device DPSI passivation. The TPV result also shows that the device with DPSI passivation had a larger average photovoltage of 1.13 V than the devices without DPSI (1.07 V), which is in accordance with the *J*–*V* measurement. The tDOS, TPV, TRPL, and PL were also tested on $FA_{0.85}MA_{0.15}Pb(Br_{0.15}I_{0.85})_3$, as shown in Figures S8–S11 (Supporting Information), and these results confirmed the conclusion that we draw from the $MAPbI_3$.

In summary, we have demonstrated the dual function of the crystallization controlling and trap states passivation enabled by sulfonic zwitterion for improving of perovskite devices. This strategy represents a new pathway toward further scalable processing of highly performance perovskite solar cells by combining of the morphology tailoring and defect passivation. The further understanding of the roles of the functional ligands in polycrystalline perovskite thin films will be beneficial for obtaining the large-scale, high uniformity, and low defect

density perovskite thin films to further move the perovskite devices toward commercialization.

Experimental Section

Spin Coating of Perovskite Films: One-step-processed $MAPbI_3$ and $FA_{0.85}MA_{0.15}Pb(Br_{0.15}I_{0.85})_3$ perovskites were fabricated by the antisolvent extraction approach in the N_2 glove box. The hole transport layer (HTL), poly(bis(4-phenyl)(2,4,6-trimethylphenyl)-amine) (PTAA), with a concentration of 2 mg mL^{-1} dissolved in toluene was spin-coated at the speed of 6000 rpm for 35 s and then annealed at 100 °C for 10 min. The $MAPbI_3$ perovskite precursor solution was prepared by dissolving 460 mg PbI_2 and 159 mg MAI in 700 µL DMF and 78 µL DMSO. The $FA_{0.85}MA_{0.15}Pb(Br_{0.15}I_{0.85})_3$ perovskite precursor solution with a concentration of 1.35 M was dissolved in mixed solvent (DMF:DMSO = 4:1). The DPSI powder was directly added to the perovskite precursor solution for the fabrication of the device with DPSI. To improve the wetting property of perovskite precursor on PTAA film, the PTAA-coated ITO substrate was prewetted by spinning 50 µL DMF at 4000 rpm for 8 s. Then 100 µL precursor solution was spun onto PTAA at 2000 rpm for 2 s and 4000 rpm for 20 s; the sample was quickly washed with 135 µL toluene at 13 s of the second-step spin coating. Subsequently, the sample was annealed at 65 °C for 10 min and 100 °C for 10 min.

Blade Coating of Perovskite Films: The $FA_{0.85}MA_{0.15}Pb(Br_{0.15}I_{0.85})_3$ perovskite solution with 0.04 wt% of DPSI for blade coating was prepared similarly with the one-step spin-coating method. The PTAA with a concentration of 2 mg mL^{-1} dissolved in toluene was spin-coated at the speed of 6000 rpm for 35 s and then annealed at 100 °C for 10 min. A drop of perovskite solution (≈10 µL) was supplied by a pipette and swiped linearly by a film applicator at a speed of ≈50 mm s^{-1} on a preheated PTAA-coated ITO/glass substrate at a 145 °C hotplate. The gap between blade and substrate was 100 µm. After coating, the perovskite film was annealed for 30 min at 100 °C.

Perovskite Solar Cell Fabrication: The PCBM dissolved in 1,2-dichlorobenzene with a concentration of 20 mg mL^{-1} was coated onto the perovskite substrate by spin coating at 6000 rpm for 35 s, and annealed at 100 °C for 30 min. The devices were finished by thermally evaporating C_{60} (20 nm), BCP (8 nm), and copper (80 nm) in sequential order.

Device Characterization: Simulated AM 1.5G irradiation (100 mW cm^{-2}) was produced by a Newport Sol3A solar simulator with a 450 W xenon source and 2 × 2 in. illuminated area for current–voltage measurements. The light intensity was calibrated by the reference cell and meter which consists of a readout device and a 2 × 2 cm calibrated solar cell made of monocrystalline silicon. The photocurrent was recorded by a Keithley Model 2400 Source-Meter with a scanning rate of 0.1 V s^{-1}. The steady-state V_{OC} and J_{SC} were measured by zero bias current and zero bias voltage versus time, respectively. The steady-state PCE was measured by monitoring current with largest power output bias voltage and recorded the value of photocurrent. XRD measurements were performed with a Rigaku D/Max-B X-ray diffractometer with Bragg–Brentano parafocusing geometry, a diffracted beam monochromator, and a conventional cobalt target X-ray tube was set to 40 kV and 30 mA. EQE curves were characterized with a Newport QE measurement kit by focusing a monochromatic beam of light onto the devices. The SEM images were taken from a Quanta 200 FEG environmental scanning electron microscope. An *LCR* (inductance (*L*), capacitance (*C*), and resistance (*R*)) meter (Agilent E4980A) was used to perform TAS measurement for the tDOS derivation. The energetic profile of tDOS can be derived from the angular-frequency-dependent capacitance using the equation

$$N_T(E_\omega) = -\frac{V_{bi}}{qW}\frac{dC}{d\omega}\frac{\omega}{k_BT} \quad (2)$$

where C is the capacitance, ω is the angular frequency, q is the elementary charge, k_B is the Boltzmann's constant, and T is the temperature. V_{bi} and W are the built-in potential and depletion width, respectively, which were extracted from the Mott–Schottky analysis. The applied angular frequency ω defines an energetic demarcation

$$E_\omega = k_BT\ln\left(\frac{\omega_0}{\omega}\right) \quad (3)$$

where the ω_0 is the attempt-to-escape frequency. The trap states below the energy demarcation can capture or emit charges with the given ω and contribute to the capacitance. For the TPV measurements, the device was serially connected to a digital oscilloscope (DOS-X 3104A) and the input impedance of the oscilloscope was set to 1 MΩ to form the open-circuit conditions, respectively, for monitoring the charge density decay. The TPV was measured under AM 1.5G illumination. An attenuated UV laser pulse (SRS NL 100 Nitrogen Laser) was used as a small perturbation to the background illumination on the device. The laser pulse–induced photovoltage variation (ΔV) and the V_{OC} were produced by the background illumination. The wavelength of the N_2 laser was 337 nm, the repeating frequency was ≈10 Hz, and the pulse width was less than 3.5 ns. The TRPL of the perovskite film was obtained in a Horiba DeltaPro fluorescence lifetime system. The excitation was provided by a DeltaDiode (DD-405) pulse laser diode with a wavelength of 404 nm. The laser excitation energy was 2 pJ $pulse^{-1}$.

Supporting Information

Supporting Information is available from the Wiley Online Library or from the author.

Acknowledgements

X.Z. and Y.D. contributed equally to this work. This work was supported by Air Force Office of Scientific Research (AFOSR) (Grant No. A9550-16-1-0299) and Office of Naval Research (ONR) (Grant No. N00014-17-1-2727).

Conflict of Interest

The authors declare no conflict of interest.

Keywords

additives, crystallization tuning, passivation, perovskite solar cells

Received: May 30, 2018
Revised: July 11, 2018
Published online: October 29, 2018

[1] Q. Dong, Y. Fang, Y. Shao, P. Mulligan, J. Qiu, L. Cao, J. Huang, *Science* **2015**, *347*, 967.
[2] M. M. Lee, J. Teuscher, T. Miyasaka, T. N. Murakami, H. J. Snaith, *Science* **2012**, *338*, 643.
[3] X. Li, D. Bi, C. Yi, J.-D. Décoppet, J. Luo, S. M. Zakeeruddin, A. Hagfeldt, M. Grätzel, *Science* **2016**, *353*, 58.
[4] S. D. Stranks, G. E. Eperon, G. Grancini, C. Menelaou, M. J. P. Alcocer, T. Leijtens, L. M. Herz, A. Petrozza, H. J. Snaith, *Science* **2013**, *342*, 341.

[5] C. Wehrenfennig, G. E. Eperon, M. B. Johnston, H. J. Snaith, L. M. Herz, *Adv. Mater.* **2014**, *26*, 1584.
[6] H. Wei, D. DeSantis, W. Wei, Y. Deng, D. Guo, T. J. Savenije, L. Cao, J. Huang, *Nat. Mater.* **2017**, *16*, 826.
[7] H. Wei, Y. Fang, P. Mulligan, W. Chuirazzi, H.-H. Fang, C. Wang, B. R. Ecker, Y. Gao, M. A. Loi, L. Cao, J. Huang, *Nat. Photonics* **2016**, *10*, 333.
[8] Z. Xiao, Y. Yuan, Y. Shao, Q. Wang, Q. Dong, C. Bi, P. Sharma, A. Gruverman, J. Huang, *Nat. Mater.* **2015**, *14*, 193.
[9] W.-J. Yin, T. Shi, Y. Yan, *Appl. Phys. Lett.* **2014**, *104*, 063903.
[10] NREL efficiency chart, https://www.nrel.gov/pv/assets/pdfs/pv-efficiencies-07-17-2018.pdf (accessed: October 2018).
[11] A. Kojima, K. Teshima, Y. Shirai, T. Miyasaka, *J. Am. Chem. Soc.* **2009**, *131*, 6050.
[12] W. S. Yang, B.-W. Park, E. H. Jung, N. J. Jeon, Y. C. Kim, D. U. Lee, S. S. Shin, J. Seo, E. K. Kim, J. H. Noh, S. I. Seok, *Science* **2017**, *356*, 1376.
[13] Y. Guo, K. Shoyama, W. Sato, E. Nakamura, *Adv. Energy Mater.* **2016**, *6*, 1502317.
[14] D. Bi, C. Yi, J. Luo, J.-D. Décoppet, F. Zhang, S. M. Zakeeruddin, X. Li, A. Hagfeldt, M. Grätzel, *Nat. Energy* **2016**, *1*, 16142.
[15] J. Jiang, Q. Wang, Z. Jin, X. Zhang, J. Lei, H. Bin, Z.-G. Zhang, Y. Li, S. (Frank) Liu, *Adv. Energy Mater.* **2018**, *8*, 1701757.
[16] H. Zhou, Q. Chen, G. Li, S. Luo, T.-b. Song, H.-S. Duan, Z. Hong, J. You, Y. Liu, Y. Yang, *Science* **2014**, *345*, 542.
[17] J.-W. Lee, H.-S. Kim, N.-G. Park, *Acc. Chem. Res.* **2016**, *49*, 311.
[18] Y. Lin, L. Shen, J. Dai, Y. Deng, Y. Wu, Y. Bai, X. Zheng, J. Wang, Y. Fang, H. Wei, W. Ma, X. C. Zeng, X. Zhan, J. Huang, *Adv. Mater.* **2017**, *29*, 1604545.
[19] N. D. Marco, H. Zhou, Q. Chen, P. Sun, Z. Liu, L. Meng, E.-P. Yao, Y. Liu, A. Schiffer, Y. Yang, *Nano Lett.* **2016**, *16*, 1009.
[20] N. K. Noel, A. Abate, S. D. Stranks, E. S. Parrott, V. M. Burlakov, A. Goriely, H. J. Snaith, *ACS Nano* **2014**, *8*, 9815.
[21] J. Peng, Y. Wu, W. Ye, D. A. Jacobs, H. Shen, X. Fu, Y. Wan, T. Duong, N. Wu, C. Barugkin, H. T. Nguyen, D. Zhong, J. Li, T. Lu, Y. Liu, M. N. Lockrey, K. J. Weber, K. R. Catchpole, T. P. White, *Energy Environ. Sci.* **2017**, *10*, 1792.
[22] M. Saliba, T. Matsui, K. Domanski, J.-Y. Seo, A. Ummadisingu, S. M. Zakeeruddin, J.-P. Correa-Baena, W. R. Tress, A. Abate, A. Hagfeldt, M. Grätzel, *Science* **2016**, *354*, 206.
[23] M. Saliba, T. Matsui, J.-Y. Seo, K. Domanski, J.-P. Correa-Baena, M. K. Nazeeruddin, S. M. Zakeeruddin, W. Tress, A. Abate, A. Hagfeldt, M. Gratzel, *Energy Environ. Sci.* **2016**, *9*, 1989.
[24] Y. Shao, Z. Xiao, C. Bi, Y. Yuan, J. Huang, *Nat. Commun.* **2014**, *5*, 5784.
[25] J. T.-W. Wang, Z. Wang, S. Pathak, W. Zhang, D. W. deQuilettes, F. Wisnivesky-Rocca-Rivarola, J. Huang, P. K. Nayak, J. B. Patel, H. A. Mohd Yusof, Y. Vaynzof, R. Zhu, I. Ramirez, J. Zhang, C. Ducati, C. Grovenor, M. B. Johnston, D. S. Ginger, R. J. Nicholas, H. J. Snaith, *Energy Environ. Sci.* **2016**, *9*, 2892.
[26] M. Yang, T. Zhang, P. Schulz, Z. Li, G. Li, D. H. Kim, N. Guo, J. J. Berry, K. Zhu, Y. Zhao, *Nat. Commun.* **2016**, *7*, 12305.
[27] H. Zhang, H. Wang, S. T. Williams, D. Xiong, W. Zhang, C.-C. Chueh, W. Chen, A. K. Y. Jen, *Adv. Mater.* **2017**, *29*, 1606608.
[28] X. Zheng, B. Chen, J. Dai, Y. Fang, Y. Bai, Y. Lin, H. Wei, X. C. Zeng, J. Huang, *Nat. Energy* **2017**, *2*, 17102.
[29] P.-W. Liang, C.-Y. Liao, C.-C. Chueh, F. Zuo, S. T. Williams, X.-K. Xin, J. Lin, A. K. Y. Jen, *Adv. Mater.* **2014**, *26*, 3748.
[30] Y. Wu, F. Xie, H. Chen, X. Yang, H. Su, M. Cai, Z. Zhou, T. Noda, L. Han, *Adv. Mater.* **2017**, *29*, 1701073.
[31] M. Yang, Z. Li, M. O. Reese, O. G. Reid, D. H. Kim, S. Siol, T. R. Klein, Y. Yan, J. J. Berry, M. F. A. M. van Hest, K. Zhu, *Nat. Energy* **2017**, *2*, 17038.
[32] W. S. Yang, J. H. Noh, N. J. Jeon, Y. C. Kim, S. Ryu, J. Seo, S. I. Seok, *Science* **2015**, *348*, 1234.
[33] J. M. Ball, A. Petrozza, *Nat. Energy* **2016**, *1*, 16149.
[34] J. Huang, Y. Yuan, Y. Shao, Y. Yan, *Nat. Rev. Mater.* **2017**, *2*, 17042.
[35] D.-Y. Son, J.-W. Lee, Y. J. Choi, I.-H. Jang, S. Lee, P. J. Yoo, H. Shin, N. Ahn, M. Choi, D. Kim, N.-G. Park, *Nat. Energy* **2016**, *1*, 16081.
[36] H. Tan, A. Jain, O. Voznyy, X. Lan, F. P. García de Arquer, J. Z. Fan, R. Quintero-Bermudez, M. Yuan, B. Zhang, Y. Zhao, F. Fan, P. Li, L. N. Quan, Y. Zhao, Z.-H. Lu, Z. Yang, S. Hoogland, E. H. Sargent, *Science* **2017**, *355*, 722.
[37] H. Uratani, K. Yamashita, *J. Phys. Chem. Lett.* **2017**, *8*, 742.
[38] Y. Yang, M. Yang, D. T. Moore, Y. Yan, E. M. Miller, K. Zhu, M. C. Beard, *Nat. Energy* **2017**, *2*, 16207.
[39] D. Zhao, Y. Yu, C. Wang, W. Liao, N. Shrestha, C. R. Grice, A. J. Cimaroli, L. Guan, R. J. Ellingson, K. Zhu, X. Zhao, R.-G. Xiong, Y. Yan, *Nat. Energy* **2017**, *2*, 17018.
[40] Z. Zhou, Z. Wang, Y. Zhou, S. Pang, D. Wang, H. Xu, Z. Liu, N. P. Padture, G. Cui, *Angew. Chem., Int. Ed.* **2015**, *54*, 9705.
[41] Y. Ding, X. Yao, X. Zhang, C. Wei, Y. Zhao, *J. Power Sources* **2014**, *272*, 351.
[42] Y. Deng, X. Zheng, Y. Bai, Q. Wang, J. Zhao, J. Huang, *Nat. Energy* **2018**, *3*, 560.
[43] Q. Wang, Q. Dong, T. Li, A. Gruverman, J. Huang, *Adv. Mater.* **2016**, *28*, 6734.
[44] H. Chen, F. Ye, W. Tang, J. He, M. Yin, Y. Wang, F. Xie, E. Bi, X. Yang, M. Grätzel, *Nature* **2017**, *550*, 92.
[45] E. Bi, H. Chen, F. Xie, Y. Wu, W. Chen, Y. Su, A. Islam, M. Grätzel, X. Yang, L. Han, *Nat. Commun.* **2017**, *8*, 15330.
[46] Y. Wu, X. Yang, W. Chen, Y. Yue, M. Cai, F. Xie, E. Bi, A. Islam, L. Han, *Nat. Energy* **2016**, *1*, 16148.
[47] T. Walter, R. Herberholz, C. Müller, H. W. Schock, *J. Appl. Phys.* **1996**, *80*, 4411.